Future Sea Level Rise and Changes on Tides in the Patagonian Continental Shelf

Author(s): Moira Luz Clara, Claudia G. Simionato, Enrique D'Onofrio, and Diego Moreira
Source: Journal of Coastal Research, 31(3):519-535.
Published By: Coastal Education and Research Foundation
DOI: http://dx.doi.org/10.2112/JCOASTRES-D-13-00127.1
URL: http://www.bioone.org/doi/full/10.2112/JCOASTRES-D-13-00127.1

Journal of Coastal Research	31	3	519–535	Coconut Creek, Florida	May 2015

Future Sea Level Rise and Changes on Tides in the Patagonian Continental Shelf

Moira Luz Clara[†]*, Claudia G. Simionato[†], Enrique D'Onofrio[‡§], and Diego Moreira[†]

[†]Centro de Investigaciones del Mar y la Atmósfera (CIMA/CONICET-UBA)
Instituto Franco-Argentino para el Estudio del Clima y sus Impactos (UMI IFAECI/CNRS-CONICET-UBA)
and Departamento de Ciencias de la Atmósfera y los Océanos, Facultad de Ciencias Exactas y Naturales (FCEN)
Universidad de Buenos Aires
Buenos Aires C1428EGA, Argentina

[‡]Servicio de Hidrografía Naval del Ministerio de Defensa
Buenos Aires C1270ABV, Argentina

[§]Instituto de Geodesia y Geofísica Aplicadas
Facultad de Ingeniería
Universidad de Buenos Aires
Buenos Aires C1127AAR, Argentina

www.cerf-jcr.org

www.JCRonline.org

ABSTRACT

Luz Clara, M.; Simionato, C.G.; D'Onofrio, E., and Moreira, D., 2015. Future sea level rise and changes on tides in the Patagonian Continental Shelf. *Journal of Coastal Research,* 31(3), 519–535. Coconut Creek (Florida), ISSN 0749-0208.

We investigate the effect of the future sea level rise (SLR) on the propagation of tides in the Patagonian Shelf by means of numerical simulations. Using a barotropic implementation of the Model for Applications at Regional Scales (MARS), we obtain solutions for scenarios which represent the present condition and potential future SLRs of 1, 2, and 10 m. The effect of flooding of low-lying areas is studied, and its influence on the propagation of tides in the region is discussed. Due to the coastal morphological features and the sense of tidal wave propagation in the Southern Hemisphere, inundation does not significantly modify the solution in the Patagonian Shelf; nevertheless, results are substantially changed in the much lower Northern Argentinean Shelf, north of 40° S, where dissipation is increased. The amplitude of M_2 responds to SLR in a spatially nonuniform manner. The response is nonlinear, particularly in regions close to the amphidromic points. Tidal dissipation by bottom friction increases consistently by 16% for the more extreme scenario with a generalized increment of tidal amplitudes, and therefore currents, over the Patagonian Shelf. Changes in the extension and position of tidal fronts are also explored. The results suggest that changes will be significant, with a reduction of the mixed areas in Cabo Blanco and San Sebastián and an increment of them in the vicinity of Península Valdés. Physical mechanisms that explain the observed modifications in the tidal regime are the changes with SLR of the speed of the tidal wave, the Rossby radius of deformation, the energy dissipation by bottom friction, and the resonant properties of the basin. Similarly to numerical studies performed for other coastal areas of the world, results indicate that important changes in the characteristics of tides can occur if SLR is large.

ADDITIONAL INDEX WORDS: *Climate change, amphidromic points, tidal fronts, tides modeling.*

INTRODUCTION

A significant global mean sea level rise (SLR) over the next decades is considered one of the more certain consequences of human-induced climate change, according to all Intergovernmental Panel on Climate Change (IPCC) assessments (*e.g.*, Meehl *et al.*, 2007; Warrick and Oerlemans, 1990). Moreover, estimations based on observations suggest that the actual increment could be larger than the IPCC-projected best-estimate rise of less than 2 mm y^{-1} (Rahmstorf, 2007). The average rate estimates have ranges of 1.8 mm y^{-1} and 5.9 mm y^{-1} (Meehl *et al.*, 2007), but some works indicate that for the 22nd century SLR could reach values as high as 15–20 mm y^{-1} (Convey *et al.*, 2009; Pfeffer, Harper, and O'Neel, 2008; Rahmstorf, 2007). The largest contributions to the rapid rise come from ocean thermal expansion (Willis, Roemmich, and Cornuelle, 2004) and melting of nonpolar glaciers. Although the ice sheet contribution has been small before, observations indicate that it is rapidly increasing, with contributions both from Greenland and Antarctica (*e.g.*, Cazenave, 2006; Rahmstorf, 2007). In related developments, the literature indicates that since the Last Glacial Maximum (18,000–22,000 years ago), rates higher than 16 mm y^{-1} have occurred (Rohling *et al.*, 2008). During those periods, significant alterations to global bathymetry by glacio-isostatic adjustment also occurred (Peltier, 2004).

Theoretically, changes in mean sea level can affect extreme sea levels indirectly by altering water depth, which modifies the propagation and dissipation of tidal energy and, presumably, the resonant properties of the basins. The effect of SLR on tides has actually been observed at several temporal scales. A number of paleo-oceanographic studies based on proxy data and numerical simulations (*e.g.*, Austin, 1991; Shaw *et al.*, 2010; Shennan *et al.*, 2000; Uehara *et al.*, 2006) show that SLR occurring since the Last Glacial Maximum has strongly affected the amplitude of tides due to changes in ocean basin bathymetry (Egbert, Ray, and Bills, 2004; Green, 2010). On shorter time scales, during the 20th and early 21st centuries, changes in ocean tides have been reported from observations over many coastal oceans (*e.g.*, Woodworth, 2010), including the Gulf of Maine (Ray, 2006), the north Atlantic (Müller, 2011; Ray, 2009), the eastern Pacific Ocean (Jay, 2009), the coasts of North America (Flick, Murray, and Ewing, 2003), and the

DOI: 10.2112/JCOASTRES-D-13-00127.1 received 19 June 2013; accepted in revision 23 October 2013; corrected proofs received 7 August 2014; published pre-print online 5 September 2014.
*Corresponding author: luzclara@cima.fcen.uba.ar

coastlines around the European Shelf (Woodworth, Shaw, and Blackman, 1991). Several hypotheses have been postulated as to the cause of the observed changes, and SLR is one of them (*e.g.*, De Ronde, 1986; Flather and Williams, 2000; Greenberg *et al.*, 2012; Haigh, Nicholls, and Wells, 2010; Howard, Lowe, and Horsburgh, 2010; Pelling and Green, 2013; Pelling, Green, and Ward, 2013; Pickering *et al.*, 2012; Roos *et al.*, 2011; Ward, Green, and Pelling, 2012; Woodworth, 2010).

The environmental, societal, and economic implications of tidal change are wide ranging, including coastal flooding, tidal renewable energy generation, sediment transport, shipping, coastal and bottom morphologic changes, changes in location of tidal mixing fronts, and changes in intertidal habitats. Therefore, those changes demand further investigation by continued analysis of historical data sets and by numerical modeling. Larger-scale changes might be of major geophysical significance, but even the regional and local ones need to be understood as far as possible if the insights obtained are to be incorporated into the tidal prediction schemes and tidal models needed for many practical purposes (Woodworth, 2010).

The bathymetry of the Patagonian Shelf (Figure l) shows a wide continental shelf with high cliffs at the coast south of 40° S, and the abrupt shelf slope is interrupted to the east of the Malvinas/Falkland Islands by the Malvinas/Falkland Plateau (Glorioso and Flather, 1997). The width of the shelf is comparable with a quarter wavelength of a semidiurnal tidal wave, thus resulting in a near-resonant natural system (Buchwald, 1980; Middleton and Bode, 1987; Webb, 1976); recent works have suggested that this is indeed the case (Arbic and Garret, 2009; Arbic, Karsten, and Garret, 2010). With its broadness, this shelf presents tidal ranges which are among the largest in the world ocean; it is also one of the regions of higher tidal dissipation by bottom friction (*e.g.*, Glorioso and Flather, 1997; Moreira, Simionato, and Dragani, 2011; Simionato *et al.*, 2004) and presents numerous tidal fronts that impact the marine ecosystem and regional fisheries (*e.g.*, Acha *et al.,* 2004; Moreira, Simionato, and Dragani, 2011; Rivas and Pisoni, 2010; Sabatini, 2004). Nevertheless, the study of potential change in tides as a consequence of SLR in this region is limited by the scarcity of long-term direct observations. Because of this, analysis of changes in tides due to SLR at a global scale (Woodworth, 2010) did not allow for any inference for this region. In this sense, numerical models are useful tools that permit not only the evaluation of potential changes but also provide insight to the mechanisms of the tidal regime change with SLR. The aim of this paper is to study the potential impact of future SLR on tidal propagation in the Patagonian continental shelf, contribute to the understanding of the mechanisms for those changes, and identify the most sensitive areas. We first analyze the SLR effect on the dominant semidiurnal tidal constituent M_2 and evaluate the linearity of the response. Then we study SLR impact on the total tide, with focus on changes from spring to neap tides. Finally we evaluate the impact of SLR on tidal frontal areas.

We applied the 2-D barotropic version of the Model for Applications at Regional Scales (MARS) developed at the French Institute for Exploitation of the Sea (IFREMER) (Lazure and Dumas, 2008; Lazure *et al.*, 2009). In the simulations we added sea level rises of 1 m, 2 m, and 10 m to the present bathymetry. The first, at a rate of 10 mm year^{-1}, is high but possible during the next century, according to the aforementioned references. The probability of an SLR of 2 m by 2100 is judged to be very low but unquantifiable (Nicholls *et al.*, 2011). It can be regarded as a possible scenario under physically possible glaciological conditions, but only if all variables are quickly accelerated to extremely high limits (Pfeffer, Harper, and O'Neel, 2008). This could be also a low- to middle-probability scenario by 2200 according to Vellinga *et al.* (2009). This value was chosen also in studies for other areas (*e.g.*, Pelling and Green, 2013; Pickering *et al.*, 2012; Ward, Green, and Pelling, 2012). An extremely high-probability hypothetical scenario was run with the aim of studying the sensitivity and linearity of the response to sea level change, as was done in other studies (*e.g.*, Pelling and Green, 2013; Pickering *et al.,* 2012; Ward, Green, and Pelling, 2012).

METHODS

The barotropic version of MARS that we used (IFREMER, 2009; Lazure and Dumas, 2008; Lazure *et al.*, 2009) was developed and distributed by the Laboratory of Physics and Sedimentology of the Department of Dynamics of the Coastal Environment at IFREMER. This code is devoted to oceanographic modeling of coastal regions and incorporates a strong environmental component. MARS has been successfully used in different applications involving diverse spatial scales and problems (see, for instance, Andre *et al.*, 2005; Lazure and Jegou, 1998; Lazure and Salomon, 1991; Muller *et al.*, 2010; Pairaud *et al.*, 2011; Pous, 2005).

Model Description and Characteristics of the Simulations

The MARS code solves hydrostatic equations for an incompressible fluid, according to the hypothesis of Boussinesq, and relies on classical finite difference schemes on an Arakawa C grid (vertical and horizontal). The vertical coordinate used is a sigma generalized coordinate. The originality of the MARS code is barotropic mode processing, evaluated semi-implicit, which eliminates time splitting. Another difference concerns the open boundary conditions, which are expressed in the center of the mesh because MARS was initially devoted to the modeling of flow forced by the tide. In the barotropic applications discussed in this paper, bottom drag is parameterized using the Strickler (inverse of the Manning) coefficient. Horizontal viscosity (v) depends upon the grid size (Δx) and on a coefficient (f_{visc}), so that $v = f_{\text{visc}} \times 0.01 \times \Delta x^{1.15}$. The model does not include any tidal conversion parameterization.

The model domain (Figure 1) spans from 60.0° S to 25.7° S and from 69.5° W to 45.5° W, completely covering the Argentinean and Uruguayan Continental Shelves, part of the Brazilian Shelf, and most of the Drake Passage. Even though this paper is focused on the Patagonian Shelf, the model domain was extended toward the north, south, and east to avoid as much as possible any boundary conditions affecting results in the study area. Egbert, Ray, and Bills (2004) show that the accuracy of the representation of tides in numerical models relies on a proper representation of bottom topography. They suggest that a model grid with a resolution higher than

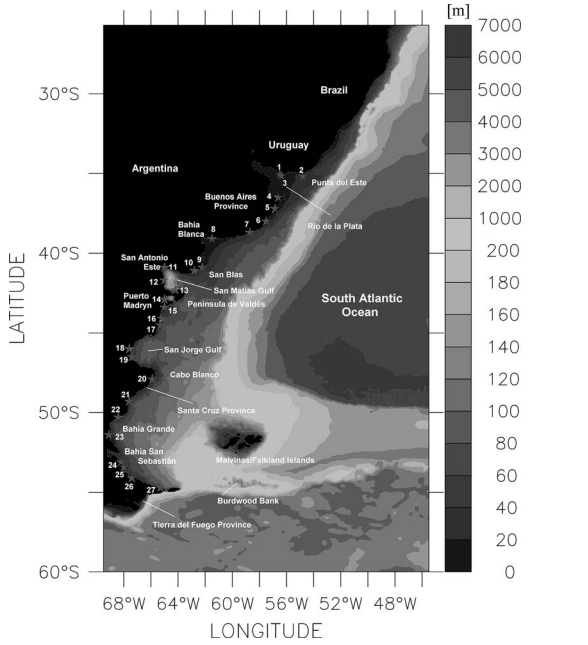

Figure 1. Domain of numerical simulations, bathymetry of the study area (in meters), and main geographical references. The stars indicate the positions of the 27 coastal stations (names and exact locations are in Table 1) used for comparison between simulations and observations and for evaluation of the results. This figure helps identify the shallow regions of the shelf where larger changes in tides properties are expected under an SLR scenario.

0.25° is required, at least for global models. In our simulations, horizontal resolution was 0.15° in longitude × 0.10° in latitude, corresponding to approximately 10 km in both directions. We used bathymetry (Figure 1) described in the project "Environmental Protection of the Río de la Plata and its Maritime Front/French Fund for the Global Environment" (FREPLATA; see FFEM, 2008). This bathymetry was derived from the digitalization of nautical charts for the shelf from the Hydrographic Service of Argentina and data from ETOPO1 (NOAA, 2008) for the deepest ocean.

Propagation of the long astronomic tidal waves in the Patagonian Shelf is computed introducing the main constituents at the open boundaries of the model. The 14 main tidal constituents (M_2, K_1, K_2, $2N_2$, M_4, MF, MM, MSQM, MTM, N_2, O_1, P_1, Q_1, and S_2) from the Aviso global Finite Element Solution model in version 2004 (FES99 [FES2004] was produced by *Legos* and *CLS* Space Oceanography Division and distributed by *Aviso*, with support from *Cnes* [http://www.aviso.oceanobs.com/]) were considered. In our simulations, following papers by Glorioso and Flather (1997), Moreira, Simionato, and Dragani (2011), and Simionato *et al*. (2004), the direct effect of the tide-generating force is not taken into account. The time step is automatically adjusted by the model to ensure numerical stability; the maximum was set to 600 seconds (10 min). The adjustment of model parameters (f_{visc} and the Manning/Strickler coefficient) to an area slightly smaller than the one considered here was done during the FREPLATA/FFEM Project and is discussed by Simionato, Moreira, Piedra-Cueva, *et al*. (2011) and Simionato, Moreira, Re, *et al*. (2011), who determined optimal values of 38 and 5, respectively. Those authors also show that this application of the model properly reproduces the main features of tide propagation in the Patagonian Shelf, including the amplitudes and phases of the main constituents, the diurnal inequalities, and the regions affected by the shallow-water constituents. In the next subsection a brief comparison of the numerical solutions to direct observations at coastal stations is presented.

All simulations were run for 18 months. The first 6 months were for model spin up and, therefore, were not analyzed. The sea surface elevations in every model node were saved every hour, and the 12 months or so of obtained data were the object of harmonic analysis following Foreman (1977).

To simplify intercomparison between simulations and, as usual in this kind of process-oriented study, in the different runs, all parameters were kept constant with the exception of the mean sea level. Simulation "T00" is the control case, in which the coastline and bathymetry correspond to present values (0 m of SLR). Simulations T01, T02, and T10 incorporate sea level rises of 1 m, 2 m, and 10 m, respectively. To help with the interpretation of the results of the diverse simulations (and following the idea proposed by Pickering *et al*. [2012]), Figure 2 shows the depth change introduced to the model in each of the SLR scenarios as a percentage of the control case depth (present sea level). Observing Figures 1 and 2 together shows the bathymetry and helps in the identification of the shallow regions of the shelf, where larger changes in tides properties are expected under an SLR scenario.

Pelling and Green (2013), Pelling, Green, and Ward (2013), and Ward, Green, and Pelling (2012) show that the way SLR is implemented in a tidal model is important for how the tides respond to the change in sea level. Their studies cover the European Shelf and the Gulf of Maine, showing that if permanent flooding of land is allowed, the response of the tides to SLR is dramatically different compared to when vertical walls are introduced at the present-day coastline—referred to as "no flooding" by Pelling, Green, and Ward (2013). This is because the newly flooded areas will have high tidal velocities due to their shallow water depth and, therefore, dissipate significant amounts of tidal energy due to bottom friction. This effect may shift the amphidromic points and, consequently, may alter the entire tidal regime. On the other hand, the introduction of high vertical walls at the present-day coastline, which of course prevents flooding of the land, not only introduces changes in the propagation speed of the tidal wave but may also impact the resonant properties of the basins (*e.g*., Arbic and Garret, 2009; Arbic, Karsten, and Garrett, 2010; Green, 2010; Pelling, Green, and Ward, 2013).

In the Patagonian Shelf high cliffs dominate the coastal landscape, and only very small low-lying areas are present at the mouths of the Gallegos, Santa Cruz, and Chubut rivers (see left panel of Figure 3); their inclusion cannot be thought *a priori* to be the cause of large changes in the response of tides. Nevertheless, northward at 40° S, the coastal morphology changes, becoming much lower and characterized by beaches and wetlands. Here, three main extensive, low-lying land areas

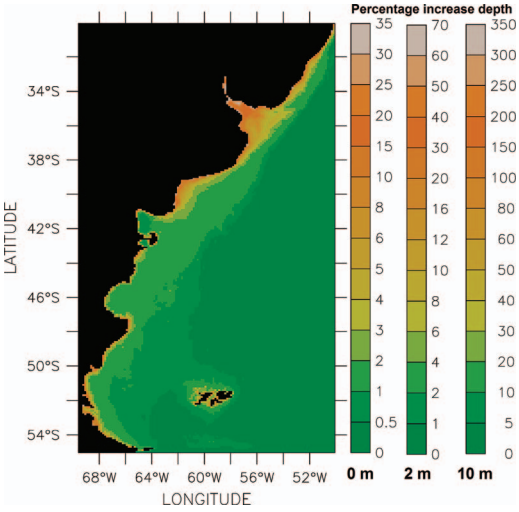

Figure 2. Percentage depth increase of the actual bathymetry for sea level rise scenarios of 1 m, 2 m, and 10 m. Note that each color bar represents a different scenario and that even though colors are maintained, they represent different percentage increases. The green and orange colors indicate areas with small and large changes, respectively. This figure shows the depth change introduced to the model in each of the SLR scenarios as a percentage of the control case depth; this helps to identify the shallow regions of the shelf, where larger changes in tides properties are expected under an SLR scenario. (Color for this figure is available in the online version of this paper.)

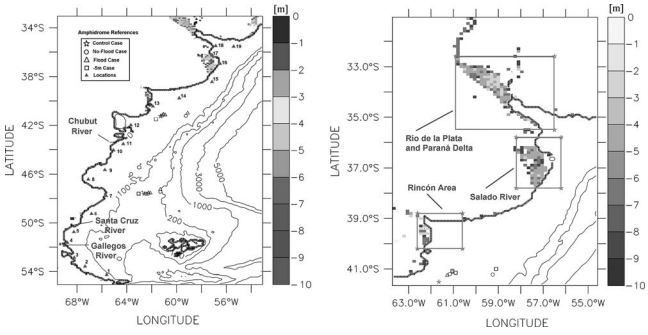

Figure 3. (left) Land topography up to 10 m, showing the grid cells that are added when the flooding of land cells is allowed in the simulations; the 19 points indicated with triangles are labeled "Site Number" in Figure 6. (right) Magnification of the northern Argentinean Shelf. Here, three main extensive, low-lying land areas that might flood under SLR can be identified: around San Blas, to the south of Samborombón Bay (in the low Salado River basin), and at the upper Río de la Plata estuary (mostly on the Paraná River delta). Figures also show locations of the amphidromes for the various simulations. The stars correspond to the control case, the squares to the –5 m SLR simulation, the circles to simulations with no flooding, and the black triangles to simulations with flooding. The amphidromes displace to the E-NE as the SLR scenario becomes more extreme.

that might flood under SLR can be identified (see right panel of Figure 3): around San Blas (in the so-called "Rincón" area), to the south of Samborombón Bay (in the low Salado River basin), and at the upper Río de la Plata estuary (mostly on the Paraná River delta). Even though these areas are not strictly the focus of this work, it is worthwhile to analyze the impact of flooding associated with SLR in potential solutions, as the above-mentioned papers have shown that the tides can be modified from remote locations. With this aim, and following the work of Pelling, Green, and Ward (2013), simulations T01, T02, and T10 were repeated in two different ways: first, by increasing the water depth over the entire region and allowing low-lying land-cells to flood (henceforth referred to as "flood runs"). Second, by increasing the water depth but not allowing new areas to flood (hereinafter denoted "no-flood runs"). No other parameter was changed between the flood and no-flood simulations.

Tidal Energetics

Important quantities that can be calculated from simulations are energy flux and dissipation by bottom friction. It is interesting to evaluate the effect of SLR on these magnitudes, as the Patagonian Shelf is one of the areas of world ocean with the largest dissipation. The energy flux can be computed as follows: (Pugh, 1987):

$$\vec{F} = (F_x, F_y) = \frac{1}{2}\rho g H A(U,V)\cos[(g_A - g_U),(g_A - g_V)], \quad (1)$$

where $\vec{F} = (F_x, F_y) = \frac{1}{2}\rho g D H_0(U,V)\cos[g_{\eta_0} - g_U, g_{\eta_0} - g_V]$ is the energy flux vector, H is the water depth, A is the amplitude of the elevation, and g_A the amplitude of its phase; (U,V) and (g_U,g_V) are the amplitude and the phase of the current components in the zonal and meridional directions, respectively, as calculated from harmonic analysis of the time series derived from the model. This formula was used by Glorioso and Flather (1997), Moreira, Simionato, and Dragani (2011), and Simionato *et al.* (2004) to estimate energy flux over the Patagonian Shelf from tidal simulations for the most important tidal constituents.

An accurate expression for estimating the mean rate of energy dissipation per unit area by bottom friction (E_b) from numerical simulations has been shown by Davies, Sauvel, and Evans 1985) to be as follows:

$$E_b = \frac{1}{T} c_b \rho \int_0^T (u_b^2 + v_b^2)^{3/2} dt, \quad (2)$$

where c_b is the bottom friction coefficient, (u_b,v_b) is the tidal bottom current, and the integration period T was chosen to be 1 year.

Limitations of the Simulations

The simulations discussed in this article include some assumptions whose consequences and limitations are extensively discussed by Pickering *et al.* (2012), who performed a similar analysis for the European Shelf. Here we will discuss them briefly and how the simulations can be justified for our particular study region.

The tidal forcing in the open boundaries of the domain is assumed not to change as a consequence of SLR. For instance, Flather and Williams (2000), Gerritsen and Berentsen (1998), Pickering *et al.* (2012), Sterl *et al.* (2009), and Ward, Green, and Pelling (2012) apply a similar approach, arguing that the relative change due to SLR in the open boundaries (where

Table 1. *Code, name, and location of the 27 coastal stations used to evaluate the results of the numerical simulations (see their locations in Figure 1).*

Station Code	Name	Latitude	Longitude
1	Montevideo[a]	−35.1	−56.5
2	Punta del Este[a]	−35.2	−54.8
3	Par Uno[a]	−35.17	−56.37
4	San Clemente[a]	−36.5	−56.6
5	Pinamar[a]	−37.2	−56.85
6	Mar del Plata[a]	−38	−57.5
7	Puerto Quequén	−38.7	−58.7
8	Monte Hermoso	−39.1	−61.5
9	San Blas[a]	−40.9	−62.2
10	Boca Río Negro	−41.1	−62.8
11	San Antonio Este[a]	−40.9	−65
12	Punta Colorada[a]	−41.7	−65
13	Golfo San José	−42.3	−64.2
14	Puerto Madryn[a]	−42.9	−65
15	Puerto Rawson	−43.4	−65
16	Punta Tombo	−44.1	−65.2
17	Santa Elena[a]	−44.5	−65.3
18	Comodoro Rivadavia[a]	−46	−67.6
19	Caleta Paula	−46.5	−67.4
20	Puerto Deseado[a]	−47.9	−65.9
21	San Julián[a]	−49.3	−67.6
22	Punta Quilla[a]	−50.3	−68.4
23	Río Gallegos[a]	−51.4	−69.1
24	Punta Vírgenes[a]	−53.1	−68.2
25	Bahía San Sebastián[a]	−53.4	−68
26	Río Grande[a]	−54.1	−67.4
27	Bahía Thetis[a]	−54.7	−65.3

[a] *Tide gauge observations are available.*

depth is high) would be small. Even though this is not strictly true in the northern portion of our model, given that almost all tidal energy reaches the domain from the south (Simionato *et al*., 2004), we assume that the associated error is negligible.

We assume, as do Flather and Williams (2000), Pickering *et al*. (2012), De Ronde (1986), and Ward, Green, and Pelling (2012), that sea level rises at the same rate everywhere—in the continental shelf and the open ocean. It could not be so in nature, but the uncertainties in spatial distribution of future SLR are too high to improve the quality of the change estimations in simulations like ours (Pickering *et al*., 2012).

Finally, no interaction between the ocean bottom and tides is allowed in our simulations. In fact, changes in the seabed might alter tidal propagation, particularly in shallow areas, and reciprocally, tides can interact with bottom sediments, producing changes on the bottom. This could be particularly important in the shallow Río de la Plata estuary, where the sediment load is very high (Moreira *et al*., 2013). Evidently, all assumptions are more applicable to a 1 m or 2 m SLR than for a 10 m SLR (Pickering *et al*., 2012).

RESULTS

In this section, results of the control simulation are first compared with tidal gauge observations and previous simulations to evaluate their performance. Then the effect of flooding of low-lying land cells under SLR on the numerical solutions is analyzed. Finally, the SLR impact on tide propagation is studied, including the effect on tidal energy and tidal fronts.

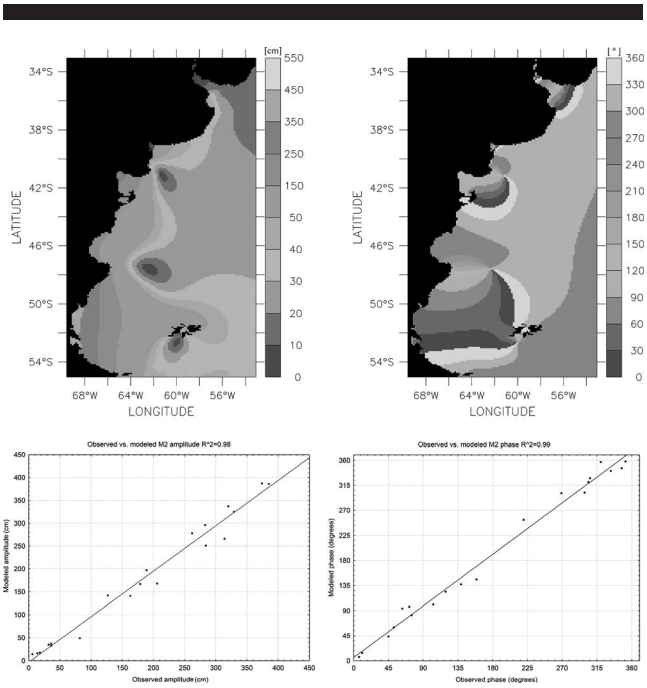

Figure 4. Cotidal charts (upper right) and isoamplitude (upper left) of the M_2 constituent obtained from control simulation T00, and scatter plots of the observed *vs*. modelled M_2 amplitude (lower left) and phase (lower right) for the control run T00 observed at the 20 coastal stations where data are available (Figure 1 and Table 1). The comparison between modeled and observed amplitudes and phases is very satisfactory, with coefficients of determination (R^2) of 0.98 and 0.99 for the amplitude and phase, respectively. In the upper-right panel three amphidromes are observed: one is located southward of the Malvinas/Falkland Islands, the second is to the east of Cabo Blanco, and the third is eastward of San Blas. A degenerated amphidrome occurs in the Río de la Plata.

Comparison with Previous Simulations and Observations

The simulation with 0 SLR (T00) corresponds to the control case, used to compare with simulations including a nonnull SLR and to verify the model's performance with the parameters proposed by Simionato, Moreira, Piedra-Cueva, *et al*. (2011) and Simionato, Moreira, Re, *et al*. (2011). With this aim, simulations were compared with tidal observations gathered at 20 coastal stations, indicated with an "a" in Table 1 and shown in Figure 1. The characteristics of these hourly tidal records are described in Simionato *et al*. (2004). The results of the comparisons are shown in the lower panel of Figure 4 as dispersion diagrams of the modeled M_2 amplitude and phase *vs*. the observed values. This constituent is the largest in the region, accounting for most of the tidal energy (see Table 2). The comparison between modeled and observed amplitudes and phases is very satisfactory, with coefficients of determination (squared correlations) of 0.98 and 0.99 for the amplitude and phase, respectively. The mean differences between simulations and observations are 0.14 m and 12.8°.

The upper panel of Figure 4 shows the cotidal and isoamplitude maps of the M_2 constituent in the region of interest obtained from the control simulation (T00) for no SLR.

Table 2. *Mean and maximum amplitudes for eight stations along the coast calculated with all the constituents, and the percentage accounted by the M_2 constituent, showing that this is the most important constituent in the analyzed region.*

Location	Mean Amplitude (m)	Maximum Amplitude (m)	% Mean Amplitude (contribution of the M_2 component)	% Maximum Amplitude (contribution of the M_2 component)
Par Uno (Canal Punta Indio, km 201.6)	0.39	0.78	89	47
Mar del Plata	0.80	1.76	93	44
Monte Hermoso	2.35	3.62	98	67
Puerto San Antonio	6.47	9.57	97	68
Puerto Madryn	3.97	5.98	95	65
Comodoro Rivadavia	4.18	6.19	95	62
Punta Quilla	7.82	12.59	98	69
Río Grande	5.41	8.67	96	63

This figure serves as a reference not only for the analysis of the changes under different SLR scenarios but also for the comparison with other simulations for the area, such as those of Glorioso (2000), Glorioso and Flather (1995, 1997), Glorioso and Simpson (1994), Moreira, Simionato, and Dragani (2011), Palma, Matano, and Piola (2004), and Simionato *et al.* (2004). Results are both qualitatively and quantitatively consistent with those of the aforementioned authors. The M_2 amplitude (upper-left panel of Figure 4) varies from less than 0.1 m along the Uruguayan coast to a maximum of around 4.5 m offshore of Santa Cruz and Tierra del Fuego provinces. A tidal wave propagates as a Kelvin wave, from south to north, leaving the coast to the left (Southern Hemisphere). Three amphidromes are observed (see upper-right panel of Figure 4): one located southward of the Malvinas/Falkland Islands, the second to the east of Cabo Blanco, and the third eastward of San Blas. Hereinafter we will refer to them as "Malvinas/Falkland Islands amphidrome," "Cabo Blanco amphidrome," and "San Blas amphidrome," respectively. When the wave reaches the shallow areas of the Río de la Plata estuary, the low depth shortens the wavelength, so that it almost fits in the estuary. It

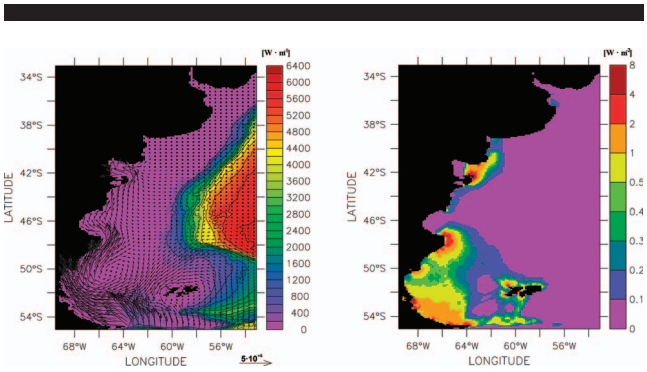

Figure 5. M_2 tidal energy flux vectors in W m^{-1} superimposed to bathymetry contours in m (left panel) and contours of total tidal energy dissipation by bottom friction in W m^{-2} (right panel) derived from the control simulation T00. Note that in the right panel the contour interval is not regular. Energy enters the domain mainly from the south, reaching the shelf through the region between Tierra del Fuego and Burdwood Bank, and from the NE, joining the main flux at approximately 52° S. It then flows northward and dissipates along the coastline, reaching the San Matías Gulf. The M_2 flux diminishes to the north, reaching very small values, indicating that energy is dissipated along the continental shelf. An integration of the energy dissipation by bottom friction over the region shown in this figure gives a result of 319 GW (1 GW = 10^9 W). (Color for this figure is available in the online version of this paper.)

is worthwhile to remark that even though it is important that the model represents the observed tide with a good degree of realism and accuracy, the objective of this paper is to compare the changes between different simulations with diverse SLRs (Pickering *et al.*, 2012).

The M_2 energy flux on the Patagonian Shelf as derived from simulation T00 is shown in the left panel of Figure 5. Given the good correspondence between simulated and observed harmonic constants, it is expected that a good estimation of this quantity would derive from model results. Glorioso and Flather (1997), Moreira, Simionato, and Dragani (2011), and Simionato *et al.* (2004) concluded that in this region, energy flux due to M_2 dominates, being two orders of magnitude larger than energy flux due to the other constituents. Our picture is qualitatively and quantitatively similar to those derived by the aforementioned authors. Energy enters the model domain mainly from the S and reaches the shelf through the region between Tierra del Fuego and Burdwood Bank. Another flux branch reaches the Malvinas/Falkland Islands from the NE. Westward of the islands this branch turns to the W and joins the main flux at approximately 52° S. It then flows northward and dissipates along the coastline, reaching the San Matías Gulf. The M_2 flux diminishes to the N, reaching very small values N of the San Matías Gulf, indicating that energy is dissipated along the continental shelf. In order to identify the most important areas for dissipation and quantify its magnitude, the mean rate of energy dissipation per unit area by bottom friction (E_b) was derived. Results for the Patagonian Shelf (right panel of Figure 5) are mostly consistent with Glorioso and Flather (1997), Moreira, Simionato, and Dragani (2011), and Simionato *et al.* (2004). Dissipation in the region is large and highly localized in four main regions: over Burdwood Bank, E of Tierra del Fuego, S of San Jorge Gulf, and at the San Matías Gulf mouth. Secondary dissipation areas are found N of San Jorge Gulf and around the Malvinas/Falkland Islands. An integration of energy dissipation by bottom friction over the region shown in Figure 5 gives a result of 319 GW (1 GW = 10^9 W). For the Patagonian Shelf, Cartwright and Ray (1989) obtained a value of 245 GW; Glorioso and Flather (1997), 218 GW; Miller (1966), 130 GW; Egbert and Ray (2000), 120 GW; Simionato *et al.* (2004), 117 GW; Moreira, Simionato, and Dragani (2011), 87 GW; and Palma, Matano, and Piola (2004), 82 GW. It must be taken into account that in every case the domains and constituents included in the analysis are different. Nevertheless, dissipation in the region constitutes an important amount of the estimated total global value (2400 GW).

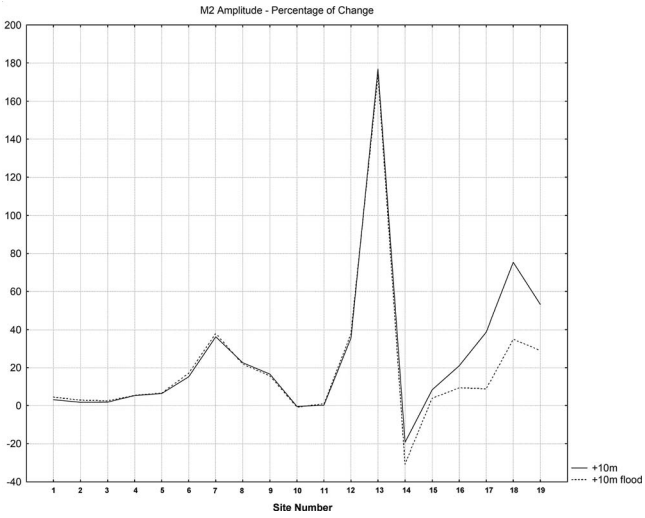

Figure 6. Percentage change of M_2 amplitude with respect to the control case T00, for the extreme case of 10 m SLR, under both flood (solid line) and no-flood (dashed line) scenarios. Values correspond to the 19 points located along the shelf from south to north (following the direction of tidal wave propagation); these locations are shown by their associated indices in the left panel of Figure 4. There is a significant reduction of M_2 amplitude to the north of San Blas when flooding of low-lying land cells is allowed.

Sensitivity to Flooding of Low-Lying Land Cells under SLR

Results indicate that no significant changes in amplitude and phase of the tide occur south of 40° S as a consequence of the flooding of low-lying land cells as sea level rises. As an example, Figure 6 shows the percentage change of M_2 amplitude with respect to the control case T00, for the extreme case of 10 m SLR, under both flood (solid line) and no-flood (dashed line) scenarios. Values correspond to the 19 points located along the shelf from south to north (following the tidal wave propagation direction), which locations are shown by their associated indices in the left panel of Figure 3. The main feature that emerges from Figure 6 is a significant reduction of M_2 amplitude to the north of San Blas when flooding of low-lying land cells is allowed. This feature and the displacement of the San Blas amphidrome to the NE in flood cases, when compared to the no-flood cases (shown in the right panel of Figure 3), are consistent with an increased bottom friction in the newly flooded land cells adjacent to the northern Argentinean Shelf. To better illustrate this point, Figure 7 shows the integrated dissipation rate by bottom friction in three boxes (shown in the right panel of Figure 3), centered at the Rincón area (blue line), the Salado River basin (red line), and the upper Río de la Plata and Paraná River delta (green line) for the control run T00 and the flood and no-flood simulations for a 10 m SLR. The dotted black line shows the addition of the integrated dissipation rates in the two last boxes. When inundation of land cells is allowed, an increase of the dissipation rate occurs when the tidal wave propagating from the south reaches the Rincón area and, particularly, the Salado River basin. In the first region an increase in dissipation by bottom friction from T00 to T10 is

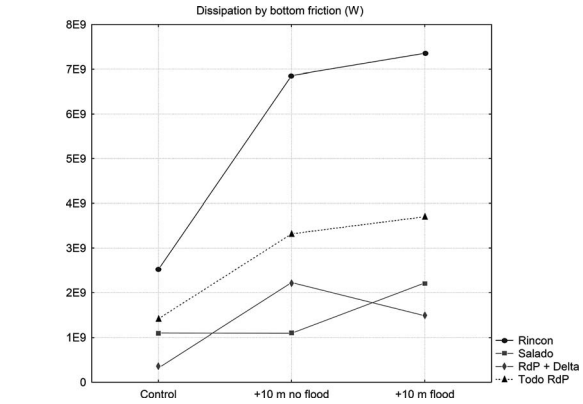

Figure 7. Integrated dissipation rate by bottom friction in three boxes (shown in the right panel of Figure 3), centered at the Rincón area (blue line), the Salado River basin (red line), and the upper Río de la Plata and Paraná River delta (green line) for the control run T00 and the flood and no-flood simulations for a 10 m SLR. The black line shows the addition of the integrated dissipation rates in the two last boxes (called "Todo RdP"). When inundation of land cells is allowed, an increase in the dissipation rate occurs when the tidal wave propagating from the south reaches the Rincón area and, particularly, the Salado River basin.

observed as a consequence of the large increments of tidal amplitudes and, therefore, currents even when no flood is allowed. When flood is permitted, dissipation is enhanced as a consequence of friction in the newly flooded shallow cells; therefore, M_2 amplitude decreases from points 13 to 14. In the Salado River basin area, the increment in dissipation occurs only in the flood run as the result of the flooding of extensive low-lying land areas. Consequently, tidal amplitude largely decreases at points 16 and 17 in the flood run when compared with the no-flood run. Note finally that when flooding is allowed, the dissipation rate in the upper Río de la Plata and Paraná delta is lower than when flooding is not allowed. This results in a generalized tidal amplitude reduction in those areas because of the increased dissipation in the Salado River basin and the Rincón, which the wave passed before. Nevertheless, as shown by the black dotted line in Figure 7, an overall increase in the tidal dissipation rate by bottom friction occurs when flooding of low-lying land cells is allowed.

To further verify our conclusions, another run was performed in which the overall depth was reduced by 5 m, reducing in this way the overall flooded area. The interpretation of the results is in this case less straightforward, as the distribution of areas with low depth changes with respect to the other runs (every wet point is 5 m shallower). It could be verified, nevertheless, that the integrated rate of dissipation by bottom friction decreases in both the Rincón area and the Río de la Plata, and consequently the San Blas amphidrome displaces to the SW, in contrast with cases in which new areas are flooded (see the right panel of Figure 3).

The way SLR is implemented does not therefore significantly modify the solution in the Patagonian Shelf due to the coastal morphological features and the sense of tidal wave propagation in the Southern Hemisphere. Nevertheless, conditions are

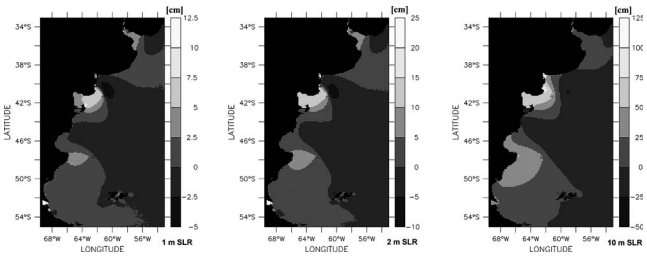

Figure 8. Variation of the amplitude of the M_2 constituent for the three SLR scenarios considered. Note that the limits of the color bars are different; this allows the degree of the linearity of the tidal response to be directly compared between the figures. If linear, the plots would be identical. The triangles and stars show the positions of the amphidromes for the current sea level scenario (0 m) and the SLR scenarios considered, respectively. All over the study area a nonlinear response occurs. The migration to the E-NE of the three amphidromes of the Patagonian Shelf and the degenerated amphidrome of the Río de la Plata, moving away from the coast, are related to changes in the spatial distribution of M_2 amplitude.

substantially changed in the northern Argentinean Shelf, characterized by extensive low-lying land areas that inundate under SLR. Therefore, given that they can be considered more reliable, only the Flood runs will be discussed when analyzing the potential effect of SLR on tides in the study area. Nevertheless it should be kept in mind that a better representation of the Río de la Plata region by means of a higher resolution would still be necessary to properly describe the changes in tides in that shallow area.

SLR and Changes in the M_2 Constituent

Contours in Figure 8 display the changes in amplitude of the M_2 constituent in the area of interest for simulations T01, T02, and T10 with respect to the control case T00. Following Pickering *et al*. (2012) and to simplify interpretation of the results, the limits of the color bars are different but proportional to the SLR; this allows the degree of linearity of the tidal response to be directly compared between the figures. If linear, the plots would be identical. In the figure, triangles and stars have been superimposed representing, respectively, the location of the amphidromes in the control simulation and their migration for each SLR scenario. Over the entire study area a nonlinear response is observed. The changes in position of the amphidromes are obviously related to changes in the spatial distribution of M_2 amplitude. The largest increments occur mainly in the region close to Cabo Blanco, between the areas south of Buenos Aires Province and north of Península Valdés, and in the Río de la Plata. The effect of SLR on tide amplification in the first two regions extends further to the north as the scenario becomes more extreme. Areas that show a reduction in tidal amplitude are the region close to Bahía Camarones, the area to the east of Bahía Blanca, and SE of Punta del Este. In the last two regions the reduction in amplitude becomes less significant as SLR becomes larger, and for the T10 scenario an increment is observed.

In regard to the position of the amphidromes, Figure 8 indicates a migration to the E-NE of the three amphidromes of the Patagonian Shelf and the degenerated amphidrome of the Río de la Plata, moving away from the coast. The observed migration is larger as the SLR scenario becomes more extreme, particularly in the case of the San Blas amphidrome. This is consistent with the increment in the Rossby radius of deformation as sea level rises, as we discuss below.

Table 3 shows the magnitude of changes in amplitude and phase of the M_2 tidal constituent, with respect to the control case, for the three SLR scenarios at the coastal stations shown in Table 1 and Figure 1. The amplitude diminishes only in two cases, Punta del Este and Monte Hermoso, for scenarios T01 and T02; it diminishes in Puerto Quequén, Puerto Madryn, and Punta Tombo for scenario T10. The largest percentage changes occur in Montevideo, Par Uno, San Blas, and Boca Río Negro. Note that the first two stations are located in the mouth of the Río de la Plata, where a degenerated (or virtual) amphidrome is located inland (Simionato *et al*., 2004). Small changes in the location of this amphidrome can produce large changes in the wave amplitude. San Blas station is much closer to the San Blas amphidrome, a position that results in the largest change; as a consequence that station is very sensitive to SLR. The same occurs for Boca Río Negro station, which is also proximate to the amphidrome. The stations located in southern Patagonia, to the south of Punta Quilla, only display small changes in amplitude, somewhat larger as the SLR increases. In most of the stations, changes in phase are negative, indicating a faster arrival of tidal wave as depth rises; this is consistent with the increment in phase speed associated with SLR, which we will discuss below.

An alternative way to evaluate the linearity of the response to SLR is to analyze the overtides. For instance, Figure 9 shows the changes in amplitude of the M_4 constituent in the area of interest for simulations T01, T02, and T10 with respect to the control case (T00). As in Figure 8, the limits of the color bars are different but proportional to SLR. In general, a reduction or increment in amplitude of M_4 as SLR increases is observed southward or northward 42° S, respectively. Nevertheless, the relative importance of this constituent becomes lower as SLR increases, being six times smaller for a 10 m SLR than for a 1 m SLR.

SLR and Changes in Spring-Neap Tides, Other Tidal Constituents, and Dissipation

Amplitudes of M_2 and S_2, amplitudes of the spring and neap tides for the control case, and the percentage change for every SLR scenario are shown in Table 4. For illustration, Figure 10 shows the change in tidal constituent S_2 for the three SLR scenarios (analogous to Figure 8 for M_2). Figure 10 shows that the response is more linear for S_2 than for M_2, whereas the change in position of the amphidromes is much smaller for S_2. Nonetheless, the response is nonlinear between Golfo San Jorge and Tierra del Fuego, to the east of San Blas, and to a lesser extent in the vicinity of Punta del Este. Note that all these sites are located close to amphidromes, either real or degenerated.

For simulation T01 larger changes in spring tide and M_2 amplitude than in neap tide are observed in 24 of the 27 analyzed stations. The three stations where the opposite occurs are Monte Hermoso, Comodoro Rivadavia, and Caleta Paula. In the T02 case, the number of stations for which the change in neap tide is less than in M_2 amplitude is 23; Punta del Este must be added to the three aforementioned stations. For the

Table 3. *Results of simulations for the 27 coastal stations. Columns show the amplitude and phase of the M_2 constituent for the control case (T00), changes observed for scenarios T01, T02, and T10, and percentage change of the amplitude. The amplitude diminishes in only two cases, Punta del Este and Monte Hermoso, for scenarios T01 and T02; for scenario T10, amplitude diminishes in Puerto Quequén, Puerto Madryn, and Punta Tombo. The largest percentage changes occur in Montevideo, Par Uno, San Blas, and Boca Río Negro. In most of the stations, changes in phase are negative, indicating a faster arrival of tidal wave as sea level rises; this is consistent with the increment in phase speed associated with SLR.*

	M_2 Amplitude (cm)				% Control Amplitude			M_2 Phase (°)			
Location	Control	+1 m SLR	+2 m SLR	+10 m SLR	+1 m SLR	+2 m SLR	+10 m SLR	Control	+1 m SLR	+2 m SLR	+10 m SLR
Montevideo	16	3	6	14	19	38	88	124	−2	−7	−60
Punta del Este	14	−1	−2	1	−7	−14	7	346	0	2	10
Par Uno	17	2	5	13	12	29	76	101	1	−1	−46
San Clemente	37	1	2	7	3	5	19	14	0	0	−13
Pinamar	35	1	2	3	3	6	9	328	0	0	−7
Mar del Plata	33	1	3	5	3	9	15	321	−2	−4	−30
Puerto Quequén	40	1	2	−4	3	5	−10	321	−6	−12	−73
Monte Hermoso	69	−2	−2	24	−3	−3	35	343	−22	−44	−157
San Blas	49	7	14	76	14	29	155	146	−8	−15	−59
San Antonio Este	266	5	12	63	2	5	24	97	−5	−10	−44
Boca Río Negro	93	7	14	67	8	15	72	122	−6	−12	−49
Punta Colorada	251	5	12	64	2	5	25	94	−5	−10	−43
Golfo San José	243	4	12	62	2	5	26	89	−5	−10	−43
Puerto Madryn	197	1	1	−3	1	1	−2	357	−3	−7	−36
Rawson	151	5	5	6	3	3	4	334	−7	−12	−37
Punta Tombo	143	0	1	−2	0	1	−1	315	−3	−8	−39
Santa Elena	141	0	1	3	0	1	2	301	−4	−8	−42
Comodoro Rivadavia	168	0	3	29	0	2	17	253	−5	−10	−50
Caleta Paula	166	0	4	31	0	2	19	249	−5	−10	−50
Puerto Deseado	167	3	7	46	2	4	28	137	−1	−3	−16
San Julián	296	1	3	36	0	1	12	82	−1	−2	−8
Punta Quilla	387	2	3	25	1	1	6	60	0	−1	−7
Río Gallegos	386	1	1	20	0	0	5	44	−1	−2	−6
Punta Vírgenes (Magallanes)	337	0	1	9	0	0	3	7	0	−1	−5
Bahía San Sebastián	325	0	0	6	0	0	2	358	0	−1	−3
Río Grande	278	1	1	6	0	0	2	341	0	0	−1
Bahía Thetis	142	0	0	1	0	0	1	302	0	0	0

T10 case, the only two stations where the change in neap tide is higher than in spring tide (~0.3 m) is Monte Hermoso.

The changes in amplitudes of M_2 and S_2 are positively correlated for all SLR scenarios, with coefficients of determination (squared correlations) of +0.4, +0.4, and +0.6 for scenarios T01, T02, and T10, respectively; this is consistent with larger changes in spring tides and M_2 amplitude than in the neap tide. When changes in the amplitudes of M_2 and S_2 are compared, in general the largest changes are observed for the M_2 constituent. The exceptions for the T01 scenario are Punta del Este, Monte Hermoso, Punta Vírgenes, and Bahía San Sebastián. For the T02 scenario, to Punta del Este, Punta Vírgenes, and Bahía San Sebastián, Puerto Madryn and Bahía Thetis must be added. For the T10 scenario, the exceptions are Puerto Quequén, Puerto Madryn, Punta Tombo, and Rawson, which show larger changes in S_2 but without a defined trend.

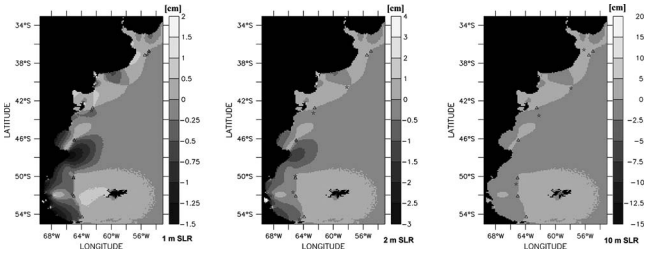

Figure 9. Variation in amplitude of the M_4 constituent for the same three SLR scenarios. Note that the limits of the color bars are different; this allows the degree of linearity of the tidal response to be directly compared between the figures. If linear, the plots would be identical. The triangles and stars show the positions of the amphidromes for the current sea level scenario (0 m) and the SLR scenarios considered, respectively. In general, a reduction (increment) in amplitude of M_4 as SLR increases is observed southward (northward) 42° S.

As scenarios with larger SLR are considered, the changes generally tend to maintain the sign. The exceptions are Punta del Este, Puerto Quequén, Monte Hermoso, Puerto Madryn, and Punta Tombo in the T10 case. This reflects the fact that changes in M_2 amplitude are larger than those of S_2 amplitude (see Table 4). For the T01 scenario there are 11 stations in which changes in the spring tide are larger than in the neap tide, 12 stations where the opposite occurs, and 3 where they are equal. For the T02 scenario, the numbers are 15, 12, and 0, respectively, and for T10, the numbers are 19, 8, and 0, respectively. From the analysis of results presented in Table 4, it is observed that, in general, areas where the percentage change in M_2 amplitude exceeds 10% are those where tidal amplitude is small. This result is consistent with the large-scale adjustment of the amphidromic system, as we will discuss in the following section.

The simulations also permit the analysis of other tidal constituents. Table 5 shows the amplitudes of the M_2, S_2, O_1,

Table 4. *Amplitude of the M_2 and S_2 tidal constituents for scenarios T01, T02, and T10 from the simulations, and impacts on the spring and neap tide. Changes show differences with respect to the control (T00) simulation and as a percentage of the amplitude of the control case. In general, areas where the percentage change in M_2 amplitude exceeds 10% are those where tidal amplitude is small.*

	M_2 Amplitude			S_2 Amplitude			$M_2 - S_2$ (neap)			$M_2 + S_2$ (spring)		
	Control	Change +1 m SLR		Control	Change +1 m SLR		Control	Change +1 m SLR		Control	Change +1 m SLR	
Location	(cm)	(cm)	%	(cm)	(cm)	%	(cm)	(cm)	%	(cm)	(cm)	%
1 m SLR[a]												
Montevideo	16	3	19	4	0	0	12	3	25	20	3	15
Punta del Este	14	−1	−7	4	0	0	10	−1	−10	18	−1	−6
Par Uno	17	2	12	4	0	0	13	2	15	21	2	10
San Clemente	37	1	3	9	0	0	28	1	4	46	1	2
Pinamar	35	1	3	9	0	0	26	1	4	44	1	2
Mar del Plata	33	1	3	8	0	0	25	1	4	41	1	2
Puerto Quequén	40	1	3	9	0	0	31	1	3	49	1	2
Monte Hermoso	69	−2	−3	24	−1	−4	45	−1	−2	93	−3	−3
San Blas	49	7	14	3	0	0	46	7	15	52	7	13
San Antonio Este	266	5	2	48	3	6	218	2	1	314	8	3
Boca Río Negro	93	7	8	11	2	18	82	5	6	104	9	9
Punta Colorada	251	5	2	45	3	7	206	2	1	296	8	3
Golfo San José	243	4	2	43	2	5	200	2	1	286	6	2
Puerto Madryn	197	1	1	46	1	2	151	0	0	243	2	1
Rawson	151	5	3	35	1	3	116	4	3	186	6	3
Punta Tombo	143	0	0	33	0	0	110	0	0	176	0	0
Santa Elena	141	0	0	32	0	0	109	0	0	173	0	0
Comodoro Rivadavia	168	0	0	35	−1	−3	133	1	1	203	−1	0
Caleta Paula	166	0	0	34	−1	−3	132	1	1	200	−1	−1
Puerto Deseado	167	3	2	31	1	3	136	2	1	198	4	2
San Julián	296	1	0	75	0	0	221	1	0	371	1	0
Punta Quilla	387	2	1	103	1	1	284	1	0	490	3	1
Río Gallegos	386	1	0	103	0	0	283	1	0	489	1	0
Punta Vírgenes (Magallanes)	337	0	0	89	1	1	248	−1	0	426	1	0
Bahía San Sebastián	325	0	0	86	1	1	239	−1	0	411	1	0
Río Grande	278	1	0	73	1	1	205	0	0	351	2	1
Bahía Thetis	142	0	0	36	0	0	106	0	0	178	0	0
	Control	Change +2 m SLR		Control	Change +2 m SLR		Control	Change +2 m SLR		Control	Change +2 m SLR	
	(cm)	(cm)	%	(cm)	(cm)	%	(cm)	(cm)	%	(cm)	(cm)	%
2 m SLR[b]												
Montevideo	16	6	38	4	1	25	12	5	42	20	7	35
Punta del Este	14	−2	−14	4	−1	−25	10	−1	−10	18	−3	−17
Par Uno	17	5	29	4	1	25	13	4	31	21	6	29
San Clemente	37	2	5	9	0	0	28	2	7	46	2	4
Pinamar	35	2	6	9	0	0	26	2	8	44	2	5
Mar del Plata	33	3	9	8	0	0	25	3	12	41	3	7
Puerto Quequén	40	2	5	9	0	0	31	2	6	49	2	4
Monte Hermoso	69	−2	−3	24	−2	−8	45	0	0	93	−4	−4
San Blas	49	14	29	3	0	0	46	14	30	52	14	27
San Antonio Este	266	12	5	48	6	13	218	6	3	314	18	6
Boca Río Negro	93	14	15	11	3	27	82	11	13	104	17	16
Punta Colorada	251	12	5	45	6	13	206	6	3	296	18	6
Golfo San José	243	12	5	43	5	12	200	7	4	286	17	6
Puerto Madryn	197	1	1	46	2	4	151	−1	−1	243	3	1
Rawson	151	5	3	35	2	6	116	3	3	186	7	4
Punta Tombo	143	1	1	33	1	3	110	0	0	176	2	1
Santa Elena	141	1	1	32	0	0	109	1	1	173	1	1
Comodoro Rivadavia	168	3	2	35	−1	−3	133	4	3	203	2	1
Caleta Paula	166	4	2	34	−1	−3	132	5	4	200	3	2
Puerto Deseado	167	7	4	31	2	6	136	5	4	198	9	5
San Julián	296	3	1	75	1	1	221	2	1	371	4	1
Punta Quilla	387	3	1	103	2	2	284	1	0	490	5	1
Río Gallegos	386	1	0	103	1	1	283	0	0	489	2	0
Punta Vírgenes (Magallanes)	337	1	0	89	2	2	248	−1	0	426	3	1
Bahía San Sebastián	325	0	0	86	2	2	239	−2	−1	411	2	0
Río Grande	278	1	0	73	1	1	205	0	0	351	2	1
Bahía Thetis	142	0	0	36	1	3	106	−1	−1	178	1	1

Table 4. *Continued.*

Location	M_2 Amplitude			S_2 Amplitude			$M_2 - S_2$ (neap)			$M_2 + S_2$ (spring)		
	Control	Change +10 m SLR		Control	Change +10 m SLR		Control	Change +10 m SLR		Control	Change +10 m SLR	
	(cm)	(cm)	%	(cm)	(cm)	%	(cm)	(cm)	%	(cm)	(cm)	%
10 m SLR[c]												
Montevideo	16	14	88	4	4	100	12	10	83	20	18	90
Punta del Este	14	1	7	4	0	0	10	1	10	18	1	6
Par Uno	17	13	76	4	3	75	13	10	77	21	16	76
San Clemente	37	7	19	9	2	22	28	5	18	46	9	20
Pinamar	35	3	9	9	1	11	26	2	8	44	4	9
Mar del Plata	33	5	15	8	3	38	25	2	8	41	8	20
Puerto Quequén	40	−4	−10	9	2	22	31	−6	−19	49	−2	−4
Monte Hermoso	69	24	35	24	−15	−63	45	39	87	93	9	10
San Blas	49	76	155	3	15	500	46	61	133	52	91	175
San Antonio Este	266	63	24	48	24	50	218	39	18	314	87	28
Boca Río Negro	93	67	72	11	18	164	82	49	60	104	85	82
Punta Colorada	251	64	25	45	23	51	206	41	20	296	87	29
Golfo San José	243	62	26	43	23	53	200	39	20	286	85	30
Puerto Madryn	197	−3	−2	46	4	9	151	−7	−5	243	1	0
Rawson	151	6	4	35	4	11	116	2	2	186	10	5
Punta Tombo	143	−2	−1	33	1	3	110	−3	−3	176	−1	−1
Santa Elena	141	3	2	32	1	3	109	2	2	173	4	2
Comodoro Rivadavia	168	29	17	35	0	0	133	29	22	203	29	14
Caleta Paula	166	31	19	34	0	0	132	31	23	200	31	16
Puerto Deseado	167	46	28	31	12	39	136	34	25	198	58	29
San Julián	296	36	12	75	8	11	221	28	13	371	44	12
Punta Quilla	387	25	6	103	6	6	284	19	7	490	31	6
Río Gallegos	386	20	5	103	4	4	283	16	6	489	24	5
Punta Vírgenes (Magallanes)	337	9	3	89	3	3	248	6	2	426	12	3
Bahía San Sebastián	325	6	2	86	3	3	239	3	1	411	9	2
Río Grande	278	6	2	73	2	3	205	4	2	351	8	2
Bahía Thetis	142	1	1	36	1	3	106	0	0	178	2	1

[a] In 11 stations changes in the spring tide are larger than in the neap tide, in 12 stations the opposite occurs, and in 3 stations they are equal. This reflects the fact that changes in M_2 amplitude are larger than those of S_2.
[b] In 15 stations changes in the spring tide are larger than in the neap tide, and in 12 stations the opposite occurs.
[c] In 19 stations changes in the spring tide are larger than in the neap tide, and in 8 stations the opposite occurs.

K_1, N_2, M_4, M_6, Q_1, P_1, and K_2 constituents for the 27 stations shown in Figure 1 and Table 1, for the control simulation T00. The most interesting feature is the relative importance of the diurnal constituents O_1 and K_1, which have larger amplitudes than S_2 in San Blas and to the north of Puerto Quequén. The changes for the various SLR scenarios (not shown) indicate that they are nonlinear and a result of the adjustment of the particular amphidromic systems. The regions where most of the constituents show large changes are Cabo Blanco, San Blas, and the Río de la Plata estuary—similar to what was observed for M_2 in the former section and related, once more, to their proximity to the amphidromes. The fact that all tidal constituents are sensitive to SLR indicates that the response to it will be larger than that shown in the previous section, when only the M_2 constituent was discussed.

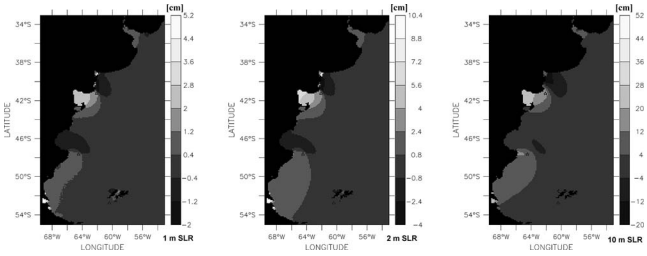

Figure 10. Variations in amplitude of the S_2 constituent for the three SLR scenarios considered. Note that the limits of the color bars are different; this allows the degree of linearity of the tidal response to be directly compared between the figures. If linear, the plots would be identical. The triangles and stars show the positions of the amphidromes for the current sea level scenario (0 m) and the SLR scenarios considered, respectively. Response is more linear for S_2 than for M_2, whereas the change in position of the amphidromes is much smaller for S_2. Nonetheless, the response is nonlinear in some sites located close to amphidromes, either real or degenerated.

Finally, the simulations also permit the estimation of changes in tidal dissipation in the Patagonian Shelf for the various SLR scenarios. The total integrated values over the area shown in the figures are 319, 324, and 369 GW for the T01, T02, and T10 scenarios, respectively, representing increases of 0%, 1.6%, and 16%. The increment is not linear, which is consistent with the generalized increment of tidal amplitudes, and therefore currents, over the Patagonian Shelf, and particularly in the regions of Cabo Blanco and offshore Península Valdés (see Figure 8), which are the areas where tidal dissipation maximizes (see Figure 5). Even though flooding of low-lying land areas with SLR increments dissipation, particularly northward of 40° S (Figure 7), the effect is minor and does not determine the overall increments observed.

Table 5. *Amplitude of tidal constituents M_2, S_2, O_1, K_1, N_2, M_4, M_6, Q_1, P_1, and K_2 at the 27 coastal stations listed in Table 1 and Figure 1 for the control case T00. Results illustrate the importance of the diurnal constituents O_1 and K_1, which have amplitudes larger than S_2 in San Blas and to the north of Puerto Quequén. The regions where most of the constituents show large changes are Cabo Blanco, San Blas, and the Río de la Plata estuary. This is related to their proximity to the amphidromes.*

Location	M_2 Amplitude (cm)	S_2 Amplitude (cm)	O_1 Amplitude (cm)	K_1 Amplitude (cm)	N_2 Amplitude (cm)	M_4 Amplitude (cm)	M_6 Amplitude (cm)	Q_1 Amplitude (cm)	P_1 Amplitude (cm)	K_2 Amplitude (cm)
Montevideo	16	4	9	7	5	2	1	2	2	1
Punta del Este	14	4	9	9	5	3	1	2	3	1
Par Uno	17	4	10	8	5	3	1	3	3	1
San Clemente	37	9	16	11	11	0	2	4	4	3
Pinamar	35	9	19	12	10	2	0	4	4	2
Mar del Plata	33	8	20	14	8	3	2	4	5	2
Puerto Quequén	40	9	17	15	7	4	1	3	5	2
Monte Hermoso	69	24	13	16	4	4	1	2	5	7
San Blas	49	3	7	12	10	3	3	1	3	1
San Antonio Este	266	48	5	9	51	2	5	1	3	13
Boca Río Negro	93	11	6	10	18	3	4	0	3	3
Punta Colorada	251	45	5	9	48	1	3	1	3	12
Golfo San José	243	43	5	9	46	1	3	1	3	11
Puerto Madryn	197	46	10	9	36	15	2	2	3	12
Rawson	151	35	11	9	27	7	5	2	3	9
Punta Tombo	143	33	13	10	24	8	1	3	3	8
Santa Elena	141	32	14	12	22	6	2	3	4	8
Comodoro Rivadavia	168	35	19	16	24	10	3	4	5	8
Caleta Paula	166	34	19	16	23	9	2	4	5	8
Puerto Deseado	167	31	23	22	37	11	2	5	7	8
San Julián	296	75	26	26	66	17	0	5	9	19
Punta Quilla	387	103	26	27	85	20	9	5	9	26
Río Gallegos	386	103	26	27	84	17	3	5	9	26
Punta Vírgenes	337	89	23	25	73	18	4	5	8	23
Bahía San Sebastián	325	86	23	24	70	20	6	5	8	22
Río Grande	278	73	21	23	60	22	7	4	8	18
Bahía Thetis	142	36	17	18	31	2	3	4	6	9

Changes in Tidal Fronts

The Patagonian Shelf presents numerous fronts due to its large extension, the diversity of water masses, and the topographic and climatological features (Guerrero and Piola, 1997). On the shelf, the tidal fronts develop in spring, summer, and fall (Bava *et al*., 2002; Carreto *et al*., 1986; Glorioso, 1987; Moreira, Simionato, and Dragani, 2011) close to Bahía Grande, Península Valdés, and Cabo Blanco. Evidently, the location and extension of those fronts can change in an SLR scenario as a consequence of changes in tidal wave propagation and depth. To analyze the change in position of tidal fronts in the Patagonian Shelf from the simulations performed in this paper, we calculated the parameter of Simpson-Hunter (Simpson and Hunter, 1974), $K = \log_{10}(H/U^3)$, where H is the depth and U is the speed. Various authors have taken different critical values of this parameter, usually between 2 and 3, as indicators of mixed areas. Here, following Moreira, Simionato, and Dragani (2011), we chose 2.5. As a reference, Figure 11 shows the distribution of the K parameter for the control case T00. In agreement with previous works based on observations and models (*e.g*., Moreira, Simionato, and Dragani, 2011; Rivas and Pisoni, 2010), the main tidal fronts occur to the NE of Península Valdés, to the NE of Cabo Blanco, and to the N of Tierra del Fuego. The three panels of Figure 12 show changes in the Simpson-Hunter parameter for those three regions, and Table 6 shows the percentage change in area of tidally mixed waters with respect to the control case, for the SLR scenarios considered. Sensitivity is observed with a tendency toward the reduction of the vertically mixed area for Cabo Blanco and San Sebastián and an increment for Península Valdés. Values are relatively high when compared with those for other areas. For instance, Ward, Green, and Pelling (2012) estimate for the European Shelf a reduction of 1% for an SLR of 2 m, whereas we find reductions of 4.4% and 3.4% for Cabo Blanco and San Sebastián, respectively. Changes can be very large for the extreme 10 m SLR scenario, exceeding 10% for San Sebastián and Península Valdés and 20% for Cabo Blanco. Those changes could have significant implications for shelf sea biogeochemistry.

DISCUSSION

A discuss of the physical mechanisms that might be responsible for changes in the tidal features observed in our numerical simulations under a potential SLR is warranted. Changes in the tidal range can be due to the increment in phase speed of the tidal wave (*e.g*., Gill, 1982; Pond and Pickard, 1983) and the barotropic Rossby radius of deformation $\left(\frac{\sqrt{gh}}{f}\right)$ (where f is the Coriolis parameter, h is the depth, and g is the acceleration due to gravity; Gill, 1982) with SLR; they can also be due to a change in energy dissipation by bottom friction in shallow regions where the relative depth change results in large (Pugh, 1987) and flooded areas (Pelling, Green, and Ward, 2013; Ward, Green, and Pelling, 2012). This has consequences on the amphidromic systems close to the coast and, potentially, on resonant semienclosed areas (Flather and Williams, 2000). Specifically, the most significant changes in

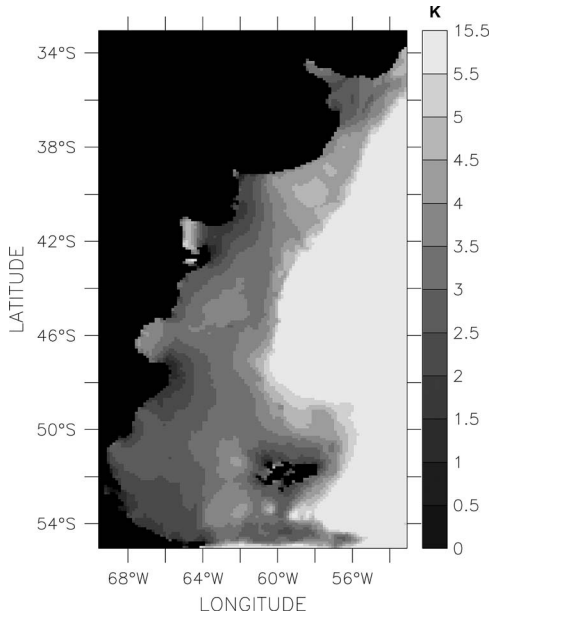

Figure 11. Contours of the Simpson-Hunter parameter derived from the control simulation for the M_2 tidal constituent. Values less than 2.5 are considered significant and are indicative of vertically mixed areas. Note that values greater than 15.5 have not been contoured. The main tidal fronts occur to the NE of Península Valdés, to the NE of Cabo Blanco, and to the N of Tierra del Fuego; a magnified view of those areas are provided in Figure 12.

tidal waves observed in the Patagonian Shelf are observed in regions close to the amphidromes, as a result of their adjustment to SLR. Similar results have been observed in simulations for other regions (*e.g.*, Pelling and Green, 2013; Pickering *et al.*, 2012; Ward, Green, and Pelling, 2012). In our simulations, a displacement of the amphidromes close to San Blas and Cabo Blanco to the E-NE is observed. A change in the degenerated amphidrome of Río de la Plata also occurs; because of the resolution of the simulations (conceived to study the shelf), however, changes in this region must be viewed with suspicion. The adjustment of the amphidromic system is precisely due to changes in the wavelength of the co-oscillating tide in the shelf (Arbic *et al.*, 2004; Pickering *et al.*, 2012). Given that the tide propagates as a long external gravity (or shallow waters) wave, with a phase speed $c = \sqrt{gh}$ (Gill, 1982), as h increases in an SLR scenario, the wave propagates faster. The wavelength λ must increase proportional to$\sqrt{h}$. In a rectangular closed basin, the first amphidrome is located to $\lambda/4$ from the boundary (Pugh, 1987), and small changes in the position of the amphidrome due to SLR might produce significant changes in the tidal range (*e.g.*, Pelling and Green, 2013; Pelling, Green, and Ward, 2013; Pickering *et al.*, 2012; Ward, Green, and Pelling, 2012). In our case, this can particularly affect the position of the amphidrome in Río de la Plata because it is a very shallow region. Given that the amplitude of the tidal wave, which propagates as a Kelvin wave, decays exponentially with distance to the coast, using a scale proportional to the barotropic Rossby radius of deformation (Gill, 1982), changes in depth also alter the position of the amphidromes in a direction normal to the coast (Pugh, 1987). This has been shown to have an effect in other areas of the coastal ocean in an SLR scenario (*e.g.*, Pelling and Green, 2013; Pelling, Green, and Ward, 2013; Pickering *et al.*, 2012; Ward, Green, and Pelling, 2012). In our case, this explains in part the displacement to the E-NE observed in the amphidromic system of the shelf. The increment in phase speed also leads to negative changes in the phase, as those observed in most stations in our simulations.

Small changes in wavelength due to depth increments because of SLR might affect the features of tides in estuaries or semienclosed areas where resonance can occur (Flather and Williams, 2000; Pelling and Green, 2013; Pelling, Green, and Ward, 2013; Pickering *et al.*, 2012; Ward, Green, and Pelling, 2012). Theoretically, estuaries and gulfs are particularly close to resonance when their length is approximately one-fourth of the tide wavelength (Pugh, 1987). If the SLR produces an increase in wave celerity, but the length of the estuary or gulf does not change, the period of oscillation might change, approximating to the period of the forcing and, therefore, producing resonance. The SLR might also cause the period of natural oscillation to move away from resonance, and in that case the tidal range might decrease. The width of the Patagonian Shelf is comparable with a quarter wavelength of a semidiurnal tidal wave (Buchwald, 1980; Middleton and Bode, 1987; Webb, 1976), and recent studies have suggested that the Patagonian Shelf would indeed be resonant (Arbic and Garret, 2009; Arbic, Karsten, and Garret, 2010). Our simulations show an increment in tidal amplitude with SLR over large portions of the shelf that might be in part related to changes in resonant properties.

Energy dissipation by bottom friction, which depends on depth, also has influence on tidal dynamics, especially in shallow areas such as the Río de la Plata estuary and the area of El Rincón (around San Blas). Similar to results observed for other coastal areas (*e.g.*, Pelling and Green, 2013; Pickering *et al.*, 2012; Ward, Green, and Pelling, 2012), when Figure 8, showing the amplitude of constituent M_2, and Figure 2, showing the relative depth change, are compared, it is observed that large increments of the M_2 amplitude occur in shallow areas, where the relative changes in depth with SLR are more significant. Our simulations show that displacement to the E-NE of the amphidromic system is due, in part, to changes in dissipation by bottom friction that occur when SLR inundates low-lying land areas.

CONCLUSIONS

The aim of this paper is to provide estimations of future tide conditions under diverse SLR scenarios for the Patagonian Shelf. We have performed a set of numerical simulations applying the regional model MARS, which reproduces the present tides with a high degree of accuracy, providing confidence in the estimation of potential future changes.

It has been shown (Pelling and Green, 2013; Pelling, Green, and Ward, 2013; Ward, Green, and Pelling, 2012) that the way tidal models are used for investigation into the impact of SLR can cause significant differences between the results. When vertical walls are added at the present coastline, the changes

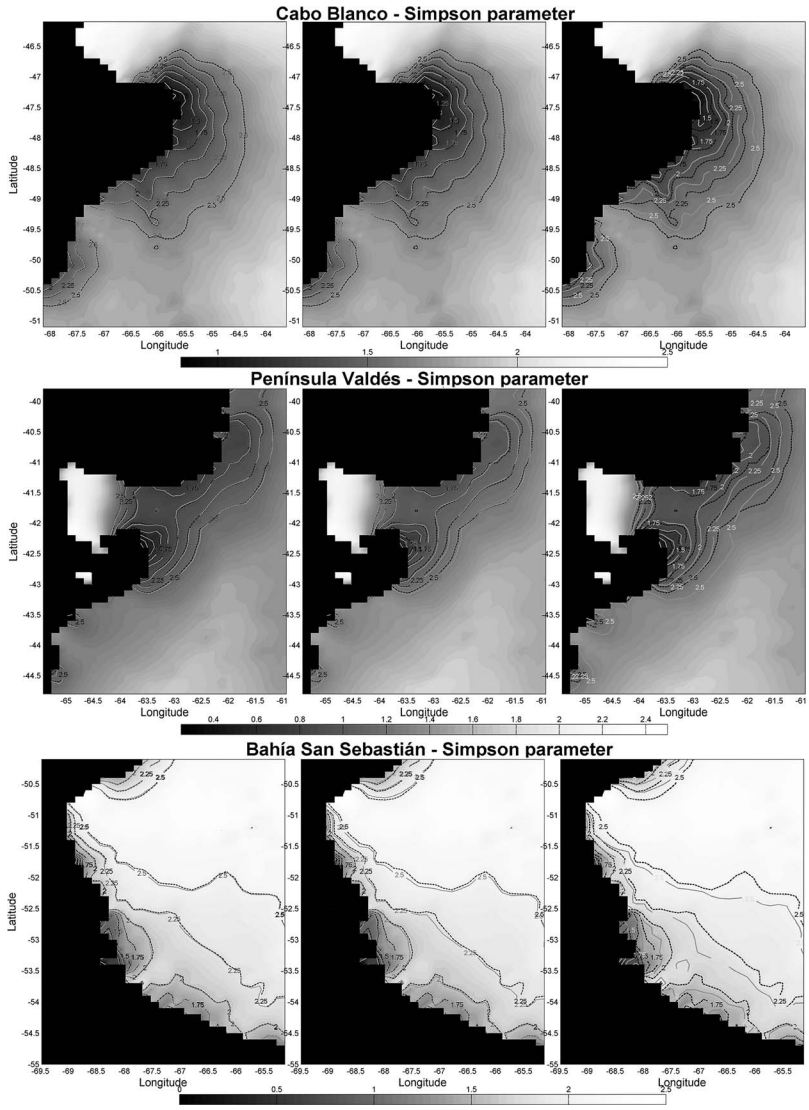

Figure 12. Simpson-Hunter parameter K for SLR scenarios of 0 m (black in all three panels), 1 m (left), 2 m (center), and 10 m (right) for the Península Valdés, Cabo Blanco, and Bahía San Sebastián regions. The gray color scale and black dashed contours correspond to the control case (0 m SLR), whereas the superimposed gray isolines display the results for the correspondent SLRs. Values less than 2.5 are considered significant and are indicative of vertically mixed areas. For an SLR scenario of 2 m, we find reductions of 4.4% and 3.4% for Cabo Blanco and San Sebastián, respectively. Changes can be very large for the extreme 10 m SLR scenario, exceeding 10% for San Sebastián and Península Valdés and 20% for Cabo Blanco.

Table 6. *Change with respect to the control case in the area of tidally mixed waters for the different SLR scenarios at the three main frontal areas of the Patagonian Shelf. Values are relatively high when compared with those found for other areas of the world ocean. Sensitivity is observed, with a tendency toward the reduction of the vertically mixed areas for Cabo Blanco and San Sebastián and an increment for Península Valdés.*

	% Change, Cabo Blanco	% Change, Península Valdés	% Change, San Sebastián
+ 1 m	−2.8	0.3	−1.9
+ 2 m	−4.4	1.0	−3.4
+ 10 m	−21.9	13.2	−10.5

are due to (subtly) changed properties of the propagating wave as water depth is altered, whereas when flooding of existing land is allowed, the response is also controlled by the newly introduced dissipation in the new cells (Pelling, Green, and Ward, 2013). The inundation of low-lying land cells can also alter the resonant properties of the basins (Pelling and Green, 2013). For this reason, prior to the analysis of the impact of SLR on tidal propagation, we studied the impact of including flooding in the simulations for the Patagonian Shelf. The coastline here is characterized by high cliffs and becomes low only northward of 40° S, where it is dominated by beaches and wetlands. In addition, the tidal wave propagates northward in the Southern Hemisphere, reaching those last low areas only

after having gone over the Patagonian Shelf. Because of this, the way SLR is implemented on the simulations has little impact in the solutions south of San Blas. North of that location the response is highly affected by added dissipation in the inundated cells, leading to a much lower effect on tidal amplitudes over the Buenos Aires province.

In regard to the impact of SLR on tidal amplitude and phase, similar studies have been addressed for other areas of the world ocean (*e.g.*, Pelling and Green, 2013; Pickering *et al.*, 2012; Ward, Green, and Pelling, 2012), and our results are quantitatively similar to them in the sense that large changes in tidal properties are to be expected if SLR is also extreme. A comparison of the simulations for SLR scenarios of 1 m, 2 m, and 10 m show that the response of M_2 amplitude is nonlinear, particularly in the areas close to San Blas and Cabo Blanco. The largest increment occurs in the area between San Blas and Golfo San José for the 10 m scenario, with a value that reaches 0.76 m. In all cases, the amphidromes displace offshore, to the E-NE, with SLR. This is the case even with the degenerated amphidrome of Río de la Plata.

In 24 of the 27 analyzed stations, the change in spring tidal range is larger than in the neap range for the 1 m SLR scenario. The same occurs in 23 of the 27 stations for the 2 m SLR scenario, and the change in spring tide is larger than in the neap tide at all stations except Monte Hermoso for the 10 m SLR scenario. Significant changes of more than 5% occur in 4, 10, and 18 of the stations for the 1 m, 2 m, and 10 m SLR scenarios, respectively. Changes of more than 10% occur in 3, 4, and 13 stations, respectively.

The most important absolute changes are observed in stations where the tidal range is larger, except for the coastal area south of Punta Quilla. To the south of San Antonio Este, the tidal constituent S_2 has a large influence on the change in tidal range, whereas north of that station (except for Monte Hermoso), the contributions of O_1 and K_1 are greater than that of S_2.

Together with a generalized increment in the tidal amplitudes over most of the Patagonian Shelf, an increase in tidal currents also occurs. This and the flooding of land areas indicates a global increment in tidal dissipation by bottom friction with SLR over that area, which reaches 16% for the extreme case of 10 m SLR.

The simulations suggest that the tidal fronts of the Patagonian Shelf will be significantly influenced by SLR. Results indicate that the global area affected by vertical mixing tends to reduce with SLR by 1.6%, 2.7%, and 8.2% for the 1 m, 2 m, and 10 m scenarios, respectively. Whereas the frontal areas of Cabo Blanco and San Sebastián tend to reduce, however, those of Península Valdés tend to increase. The most sensitive region is Cabo Blanco, where the reduction in vertically mixed areas is –2.8%, –4.4%, and –21.9% for 1 m, 2 m, and 10 m SLR, respectively.

The physical mechanisms that explain the observed modifications in the tidal regime are SLR-induced changes in: (1) the speed of the tidal wave, (2) the Rossby radius of deformation, (3) energy dissipation by bottom friction, and (4) the resonant properties of the basin. These changes produce the migration of the amphidromes and complex nonlinear patterns of change in tidal waves.

ACKNOWLEDGMENTS

This study was funded by projects of the Agencia Nacional de Promoción Científica y Tecnológica in Argentina (PICT 2010-1831), the Consejo Nacional de Investigaciones Científicas y Técnicas in Argentina (CONICET, PIP 112 201101 00176), and the Secretaría de Ciencia y Técnica of University of Buenos Aires (UBACyT) (2011–2014 20020100100840). The participation of Moira Luz Clara Tejedor and Diego Moreira was allowed by CONICET and University of Buenos Aires Ph.D. fellowships, respectively. The authors are grateful to Reviewer 3 for his or her careful reading of the manuscript and constructive comments and suggestions, which contributed to a significant improvement of this work.

LITERATURE CITED

Acha, E.M.; Mianzan, H.W.; Guerrero, R.A.; Favero, M., and Bava, J., 2004. Marine fronts at the continental shelves of austral South America, physical and ecological processes. *Journal of Marine Systems*, 44(1–2), 83–105.

Andre, G.; Garreau P.; Garnier V., and Fraunié, P., 2005. Modelled variability of the sea surface circulation in the north-western Mediterranean Sea and in the Gulf of Lions. *Ocean Dynamics*, 55, 294–308.

Arbic, B.K.; Garner, S.T.; Hallberg, R.W., and Simmons, H.L., 2004. The accuracy of surface elevations in forward global barotropic and baroclinic tide models. *Deep-Sea Research Part II: Topical Studies in Oceanography*, 51, 3069–3101.

Arbic, B.K. and Garrett, C., 2009. A coupled oscillator model of shelf and ocean tides. *Continental Shelf Research*, 30(6), 564–574.

Arbic, B.K.; Karsten, R.H., and Garret, C., 2010. On tidal resonance in the global ocean and the back-effect of coastal tides upon open-ocean tides. *Atmosphere-Ocean*, 47(4), 239–266.

Austin, R.M., 1991. Modelling Holocene tides on the NW European continental shelf. *Terra Nova*, 3, 276–288.

Bava, J.; Gagliardini, D.A.; Dogliotti, A.I., and Lasta, C.A., 2002. Annual distribution and variability of remotely sensed sea surface temperature fronts in the south-western Atlantic Ocean. *Proceedings of the 29th International Symposium on Remote Sensing of the Environment* (Buenos Aires, Argentina, International Center for Remote Sensing of Environment), pp. 1–6.

Buchwald, V.T., 1980. Resonance of Poincaré waves on a continental shelf. *Australian Journal of Marine and Freshwater Research*, 31, 451–457.

Carreto J.I.; Benavides, H.R.; Negri, R.M., and Glorioso, P.D., 1986. Toxic red tide in the Argentine Sea. Phytoplankton distribution and survival of the toxic dinoflagellate *Gonyaulax excavata* in a frontal area. *Journal of Plankton Research*, 8, 15–28.

Cartwright, D.E. and Ray, R.D., 1989. New estimates of oceanic tidal energy dissipation from satellite altimetry. *Geophysical Research Letters*, 16(1), 73–76.

Cazenave A., 2006. Atmosphere: How fast are the ice sheets melting? *Science*, 314(5803), 1250–1252.

Cnes. *Aviso+ Satellite Altimetry Data*. http://www.aviso.oceanobs.com/.

Convey, P.; Bindschadler, R.; di Prisco, G.; Fahrbach, E.; Gutt J.; Hodgson, D.A.; Mayewski, P.A.; Summerhayes, C.P., and Turner, J., 2009. Antarctic climate change and the environment. *Antarctic Science*, 21, 541–563.

Davies, A.M.; Sauvel, J., and Evans, J., 1985. Computing near coastal tide dynamics from observations and a numerical model. *Continental Shelf Research*, 4, 341–366.

De Ronde, J.G., 1986. Bepaling Knoopfactoren Harmonische Analyse met het Continental Shelf Model. *Rijkswaterstaat, Dienst Getijdewateren*. Notitie GWAO, 86.309. 250p.

Egbert, G.D. and Ray, R.D., 2000. Significant dissipation of tidal energy in the deep ocean inferred from satellite altimeter data. *Nature*, 405, 775–778.

Egbert, G.D.; Ray, R.D., and Bills, B.G., 2004. Numerical modeling of the global semidiurnal tide in the present day and in the last

glacial maximum. *Journal of Geophysical Research*, 109 (C03003), 15.

FFEM (French Fund for the Global Environment). *Proyecto* "*Reducción y Prevención De la Cantaminación de origen terrestre en el Río de la Plata y su Frente Marítimo mediante la implementación del Programa de Acción Estratégico de Freplata*". http://www.freplata.org.

Flather, R.A. and Williams, J.A., 2000. Climate change effects on storm surges: methodologies and results. *In:* Beersma, J.; Agnew, M.; Viner, D., and Hulme, M., *et al*. (eds.), *Climate Scenarios for Water Related and Climate Impacts*. ECLAT-2 Workshop Report No. 3, KNMI, The Netherlands (May 10–12, 2000). Norwich, United Kingdom: Climate Research Unit, pp. 66–78.

Flick, R.E.; Murray, J.F., and Ewing, L.C., 2003. Trends in United States tidal datum statistics and tide range. *Journal of Waterway, Port, Coastal, and Ocean Engineering—ASCE*, 129, 155–164.

Foreman, M.G.G., 1977. Manual for Tidal Heights Analysis and Prediction. Patricia Bay, Sidney, B.C., Canada. *Pacific Marine Science Report* 77–10. Sidney, B.C., Canada: Institute of Ocean Science, 97p.

Gerritsen, H. and Berentsen, C.W.J., 1998. A modelling study of tidally induced equilibrium sand balances in the North Sea during the Holocene. *Continental Shelf Research*, 18, 151–200.

Gill, A., 1982. *Atmosphere-Ocean Dynamics*. San Diego, California: Academic, 662p.

Glorioso, P.D., 1987. Temperature distribution related to shelf-sea fronts on the Patagonian shelf. *Continental Shelf Research*, 7(1), 27–34.

Glorioso, P.D., 2000. Patagonian Shelf 3-D tide and surge model. *Journal of Marine Systems*, 24, 141–151.

Glorioso, P.D. and Flather, R.A., 1995. A barotropic model of the currents off SE South America. *Journal of Geophysical Research*, 100, 13427–13440.

Glorioso, P.D. and Flather, R.A., 1997. The Patagonian Shelf tides. *Progress in Oceanography*, 40, 263–283.

Glorioso, P.D. and Simpson, J.H., 1994. Numerical modelling of the M_2 tide on the northern Patagonian shelf. *Continental Shelf Research*, 14, 267–278.

Green, J., 2010. Ocean tides and resonance. *Ocean Dynamics*, 60, 1243–1253.

Greenberg, D.A.; Blanchard, W.; Smith, B., and Barrow, E., 2012. Climate change, mean sea level rise and high tides in the Bay of Fundy. *Atmosphere-Ocean*, 50(3), 1–16. doi:10.1080/07055900.2012.668670

Guerrero, R.A. and Piola, A.R., 1997. Masas de agua en la plataforma continental. *In:* Boschi, E.E. (ed.), *El Mar Argentino y sus Recursos Pesqueros. Antecedentes Históricos de las Exploraciones en el Mar y las Características Ambientales*. Volume 1. Mar del Plata, Argentina: Instituto Nacional de Investigaciones y Desarrollo Pesquero, pp. 107–118.

Haigh, I.; Nicholls, R., and Wells, N., 2010. Assessing changes in extreme sea levels: application to the English Channel, 1900–2006. *Continental Shelf Research*, 30, 1042–1055.

Howard, T.; Lowe, J., and Horsburgh, K., 2010. Interpreting century-scale changes in southern North Sea storm surge climate derived from coupled model simulations. *Journal of Climate*, 23, 6234–6247.

IFREMER (French Institute for Exploitation of the Sea). *Model for Applications at Regional Scale*. http://wwz.ifremer.fr/mars3d.

Jay, D.A., 2009. Evolution of tidal amplitudes in the eastern Pacific Ocean. *Geophysical Research Letters*, 36, L04603.

Lazure, P. and Dumas, F., 2008. An external-internal mode coupling for a 3D hydrodynamic model for applications at regional scale (MARS). *Advances in Water Resources*, 31(2), 233–250.

Lazure, P.; Garnier, V.; Dumas, F.; Herry, C., and Chiffl, M., 2009. Development of a hydrodynamic model of the Bay of Biscay. Validation of hydrology. *Continental Shelf Research*, 29(8), 985–997.

Lazure, P. and Jegou, A.M., 1998. 3D modelling of seasonal evolution of Loire and Gironde plumes on Biscay continental shelf. *Oceanologica Acta*, 21(2), 165–177.

Lazure, P. and Salomon, J.C., 1991. Etude par modeles mathématiques de la circulation marine entre Quiberon et Noirmoutier. Actes du colloque international sur l'environnement des mers épicontinentales. *Oceanologica Acta*, 11, 93–99.

Meehl, G.A.; Stocker, T.F.; Collins, W.D.; Friedlingstein, P.; Gaye, A.T.; Gregory, J.M.; Kitoh, A.; Knutti, R.; Murphy, J.M.; Noda, A.; Raper, S.C.B.; Watterson, I.G.; Weaver, A.J., and Zhao, Z.-C., 2007. Global climate projections. *In:* Solomon, S.; Qin, M.D.; Manning, M.; Chen, Z.; Marquis, M.; Averyt, K.B.; Tignor, M., and Miller, H.L., (eds.), *Climate Change 2007: The Physical Science Basis. Contribution of Working Group 1 to the Fourth Assessment Report of the Intergovernmental Panel on Climate Change, 2007*. Cambridge, United Kingdom: Cambridge University Press, pp. 747–845.

Middleton, J.H. and Bode, L., 1987. Poincaré waves obliquely incident to a continental shelf. *Continental Shelf Research*, 7, 177–190.

Miller, G.R., 1966. The flux of tidal energy out of the deep oceans. *Journal of Geophysical Research*, 71, 2485–2489.

Moreira, D.; Simionato, C.G., and Dragani, W., 2011. Modeling ocean tides and their energetics in the North Patagonia Gulfs of Argentina. *Journal of Coastal Research*, 27(1), 87–102.

Moreira, D.; Simionato, C.G.; Gohin, F.; Cayocca, F., and Luz Clara Tejedor, M., 2013. Suspended matters mean distribution and seasonal cycle in the Río de la Plata estuary and the adjacent shelf from MODIS and in situ observations. *Continental Shelf Research*, 68, 51–66.

Müller, M., 2011. Rapid change in semi-diurnal tides in the North Atlantic since 1980. *Geophysical Research Letters*, 38, L11602.

Muller, H.; Blanke, B.; Dumas, F., and Mariette, V., 2010. Identification of typical scenarios for the surface Lagrangian residual circulation in the Iroise Sea. *Journal Of Geophysical Research—Oceans*, 115, C07008. doi: 10.1029/2009JC005834

Nicholls, R.J.; Marinova, N.; Lowe, J.A.; Brown, S.; Vellinga, P.; De Gusmao, D.; Hinkel, J., and Tol, R.S.J., 2011. Sea-level rise and its possible impacts given a "beyond 4 degrees C world" in the twenty-first century. *Philosophical Transactions of the Royal Society of London. Series A. Mathematical, Physical and Engineering*, 369, 161–181.

NOAA (National Ocean and Atmospheric Administration). *ETOPO1 Global Relief Model*. http://www.ngdc.noaa.gov/mgg/global/global.html.

Pairaud I.; Gatti J.; Bensoussan N.; Verney R., and Garreau, P., 2011. Hydrology and circulation in a coastal area off Marseille: validation of a nested 3D model with observations. *Journal of Marine Systems*, 88(1), 20–33. doi: 10.1016/j.jmarsys.2011.02.010

Palma, E.D.; Matano, R.P., and Piola, A.R., 2004. A numerical study of the southwestern Atlantic Shelf circulation: barotropic response to tidal and wind forcing. *Journal of Geophysical Research*, 109, C08014. doi:10.1029/2004JC002315

Pelling, H.E and Green, J.A.M., 2013. Sea level rise, tidal power and resonance in the Gulf of Maine. *Journal of Geophysical Research*, 118, 2863–2873. doi:10.1002/jgrc.20221

Pelling, H.E.; Green, J.A.M., and Ward, S.L., 2013. Modelling tides and sea-level rise: to flood or not to flood. *Ocean Modelling*, 63, 21–29. doi:10.1016/j.ocemod.2012.12.004

Peltier, W.R., 2004. Global glacial isostasy and the surface of the ice-age earth: the ice-5G (VM2) model and GRACE. *Annual Review of Earth and Planetary Sciences*, 32, 111–149.

Pfeffer, W.T.; Harper, J.T., and O'Neel, S., 2008. Kinematic constraints on glacier contributions to 21st century sea-level rise. *Science*, 321, 1340–1343.

PHYSED (Laboratoire de la Physique Hydrodynamique et Sédimentaire). *Team description*. http://wwz.ifremer.fr/dyneco/Teams/PHYSED.

Pickering, M.D.; Wells, N.C.; Horsburgh, K.J., and Green, J.A.M., 2012. The impact of future sea-level rise on the European Shelf tides. *Continental Shelf Research*, 35, 1–15. doi:10.1016/j.csr.2011.11.011

Pond, S. and Pickard, G.L., 1983. *Introductory Dynamical Oceanography*, 2nd edition. Oxford, England: Pergamon Press Ltd., 349p.

Pous, S., 2005. Dynamique Océanique dans les Golfes Persique et d'Oman. Brest Cedex, France: Université de Bretagne Occidentale, These de doctorat, 178p.

Pugh, D., 1987. *Tides, Surges and Mean Sea-Level*. Chichester, United Kingdom: Wiley, 472p.

Rahmstorf, S., 2007. A semi-empirical approach to projecting future sea-level rise. *Science*, 315, 368–370.

Ray, R.D., 2006. Secular changes of the M_2 tide in the Gulf of Maine. *Continental Shelf Research*, 26, 422–427.

Ray, R.D., 2009. Secular changes in the solar semidiurnal tide of the western North Atlantic Ocean. *Geophysical Research Letters*, 36, L19601. doi:10.1029/2009GL040217

Rivas, A.L. and Pisoni, J.P., 2010. Identification, characteristics and seasonal evolution of surface thermal fronts in the Argentinean Continental Shelf. *Journal of Marine Systems*, 79(1–2), 134–143.

Rohling, E.J.; Grant, K.; Hemleben, C.; Siddall, M.; Hoogakker, B.A.A.; Bolshaw, M., and Kucera, M., 2008. High rates of sea-level rise during the last interglacial period. *Nature Geoscience*, 1, 39–42.

Roos, P.C.; Velema, J.J.; Hulscher, S.J.M.H., and Stolk, A., 2011. An idealized model of tidal dynamics in the North Sea: resonance properties and response to large-scale changes. *Ocean Dynamics*, 61(12), 2019–2035. doi:10.1007/s10236-011-0456-x

Sabatini, M.E., 2004. Características ambientales, reproducción y alimentación de la merluza (*Merluccius hubbsi*) y la anchoíta (*Engraulis anchoíta*) en su hábito reproductivo patagónico. Síntesis y perspectivas. *Revista de Investigación y Desarrollo Pesquero, Argentina*, 16, 5–25.

Shaw, J.; Amos, C.L.; Greenberg, D.A.; O'Reilly, C.T.; Parrott, D.R., and Patton, E., 2010. Catastrophic tidal expansion in the Bay of Fundy, Canada. *Canadian Journal of Earth Sciences*, 47, 1079–1091.

Shennan, I.; Lambeck, K.; Flather, R.; Horton, B.; McArthur, J.; Innes, J.; Lloyd, J.; Rutherford, M., and Wingfield, R., 2000. Modelling western North Sea palaeogeographies and tidal changes during the Holocene. *Geological Society, London Special Publications*, 166, 299–319.

Simionato, C.G.; Dragani, W.; Nuñez, M., and Engel, M., 2004. A set of 3-D nested models for tidal propagation from the Argentinean Continental Shelf to the Río de La Plata Estuary, Part I M2. *Journal of Coastal Research*, 20(3), 893–912.

Simionato, C.G.; Moreira, D.; Piedra-Cueva, I.; Fossati, M.; Re, M.; Sabarots-Gerbet, M.; Menendez, A., and Cayocca, F., 2011. Proyecto FREPLATA–FFEM modelado numérico y mediciones in situ y remotas de las transferencias de sedimentos finos a través del Río de la Plata. Parte B: Simulaciones numéricas. *Frente Marítimo*, 22, 137–176.

Simionato, C.G.; Moreira, D.; Re, M., and Fossati, M., 2011. Estudio de la Dinámica Hidro-sedimentológica del Río de la Plata: Observación y Modelación Numérica de los Sedimentos Finos. *Publicación Proyecto FREPLATA, CTMFM-CARP*, 109p.

Simpson, J.H. and Hunter, J., 1974. Fronts in the Irish Sea. *Nature*, 250, 404–406.

Sterl, A.; van den Brink, H.; de Vries, H.; Haarsma, R., and van Meijgaard, E., 2009. An ensemble study of extreme storm surge related water levels in the North Sea in a changing climate. *Ocean Science*, 5, 369–378.

Uehara, K.; Scourse, J.D.; Horsburgh, K.J.; Lambeck, K., and Purcell, A.P., 2006. Tidal evolution of the northwest European shelf seas from the Last Glacial Maximum to the present. *Journal of Geophysical Research C: Oceans*, 111, C09025.

Vellinga, P.; Katsman, C.A.; Sterl, A.; Beersma, J.J.; Church, J.A.; Hazeleger, W.; Kopp, R.E.; Kroon, D.; Kwadijk, J.; Lammersen, R.; Lowe, J.; Marinova, N.; Oppenheimer, M.; Plag, H.P.; Rahmstorf, S.; Ridley, J.; von Storch, H.; Vaughan, D.G.; van der Wal, R.S.W., and Weisse, R., 2009. Exploring High-End Climate Change Scenarios for Flood Protection of the Netherlands. Alterra, the Netherlands: KNMI. *Scientific Report WR, International scientific assessment carried out at request of the Delta Committee*, 144p.

Ward, S.; Green, J.A.M., and Pelling, H.E., 2012. Tides, sea-level rise and tidal power extraction on the European shelf. *Ocean Dynamics*, 62, 1153–1167. doi:10.1007/s10236-012-0552-6

Warrick, R.A. and Oerlemans, J., 1990. Sea level rise. *In:* Houghton, J.T.; Jenkins, G.J., and Emphraums, J.J. (eds.), *Climate Change. The Intergovernmental Panel on Climate Change First Assessment Report*. Cambridge, United Kingdom: Cambridge University Press, pp. 261–281.

Webb, D.J., 1976. A model of continental-shelf resonances. *Deep Sea Research*, 23, 1–15.

Willis, J.K.; Roemmich, D., and Cornuelle, B., 2004. Interannual variability in upper ocean heat content, temperature, and thermosteric expansion on global scales. *Journal of Geophysical Research C: Oceans*, 109(12), 1–13.

Woodworth, P.L., 2010. A survey of recent changes in the main components of the ocean tide. *Continental Shelf Research*, 30, 1680–1691.

Woodworth, P.L.; Shaw, S.M., and Blackman, D.B., 1991. Secular trends in mean tidal range around the British Isles and along the adjacent European coastline. *Geophysical Journal International*, 104, 593–610.